Brittle ice shell thickness of Enceladus from fracture distribution analysis

A. Lucchetti[1*], R. Pozzobon[2*], F. Mazzarini[3], G. Cremonese[1], M. Massironi[2,1]

[1] INAF-Astronomical Observatory of Padova, Vicolo dell'Osservatorio 5, 35131 Padova, Italy.

[2] Dipartimento di Geoscienze, Università di Padova, Padova, Italy.

[3] Istituto Nazionale di Geofisica e Vulcanologia, Via Della Faggiola 32, 56100, Pisa, Italy.

Corresponding author: Alice Lucchetti (alice.lucchetti@oapd.inaf.it)

* These authors equally contributed to this work

Keywords: Enceladus; Satellites, surface; geological processes.

Highlights:

- Brittle ice shell thickness calculated for the SPT is approximately 31 km
- The ice depth of fracture penetration increases from 31 km to 70 km up to 75°N
- We demonstrate the prevalence of fractal populations of faults on Enceladus

Abstract

We determine the depth of fracture penetration in multiple regions of Enceladus by performing self-similar clustering and length distribution analysis of fractures. The statistical characterization of fault-population attribute, such as length and clustering, provide a productive avenue for exploring deformation rate, stress transmission mode, rheology of the medium, and mechanical stratification of the ice satellite. Through this analysis, we estimate the depth of the mechanical discontinuity of Enceladus' ice shell that is the depth to which fractures penetrate the brittle ice layer above the ductile one.

In this work, we find that for the South Polar Terrain (SPT), the brittle ice shell interested by fracture penetration is about 30 km and corresponds to the total depth of the ice shell because the SPT has a very high thermal gradient and, hence, fractures likely reach the ocean-ice interface. In the other regions analyzed, the depth of fracture penetration increases from 31 to 70 km from the South Pole to northern regions up to 75°.

1 Introduction

Enceladus is the smallest Solar System body that presents intense geologic activity on its surface. It is a heavily deformed satellite **with** a visible geological history stretching from billion of years ago to the present. The **geologically-youngest** region of the satellite is the strongly fractured area surrounding the South Pole, called **the** South Pole Terrain (hereafter SPT). The numerous cracks in the SPT **appear** to be directly related to high-energy effusive activity of vapor plumes revealed **in** images taken by the NASA Cassini spacecraft (Hansen et al., 2006; Porco et al., 2006; Porco et al., 2014). The SPT **equally-spaced**, tension fractures are known as "tiger stripes" (Yin and Pappalardo, 2015; Yin et al., 2016) and are in correspondence **with** high rates of heat flow indicated by thermal measurements (Spencer et al., 2006). The geologically active SPT has been interpreted as evidence of a liquid water reservoir beneath the South Pole (Collins and Goodman, 2007), and most likely below the entire ice crust (Patthoff and Kattenhorn, 2011). Estimates of the SPT total ice shell thickness have been derived using gravity and physical libration data, **with** values between 15 and 40 km (Iess et al., 2014; McKinnon, 2015, Thomas et al., 2016). The determination of the total ice shell thickness of Enceladus has important implications for both **its** thermal history and astrobiological potential. However, the mechanical boundary between the ice layer and ocean is not discrete, rather, the brittle ice layer is underlained by ductile ice that deforms in accordance with satellite strain rates and thermal gradients (Roberts and Nimmo, 2008). Temperatures near the surface of Enceladus are sufficiently cold and overburden pressures **are** sufficiently small that tectonic stresses are likely to result in brittle deformation exhibiting evidence of extensional deformation and **strike-slip** faulting.

The analysis of faults and fault populations on the icy satellite can reveal insight into the evolution of its surface that cannot be gained from other techniques. Statistical characterization of fault-population attributes, such as length and clustering, provide a productive avenue for exploring deformation rate**s**, stress transmission mode**s**, rheology of the medium**,** and mechanical stratification (e.g. Benedicto et al., 2003; Soliva and Schultz, 2008; Gudmundsson et al. 2010; Schultz et al., 2010; Gudmundsson et al. 2013).

For instance, fractal analysis has been utilized in terrestrial studies to determine the thickness of the fractured (brittle) crust (e.g., Mazzarini and D'Orazio, 2003; Mazzarini, 2004; Soliva and Schultz, 2008; Mazzarini and Isola, 2010). Similarly, on Enceladus we can constrain the depth at which fractures penetrate the brittle ice layer exploring some of the main characteristics of fault populations **such** as length and clustering. We provide thickness estimates of Enceladus' **brittle** ice crust in multiple regions using a structural geology approach that employs fractures**'** self-

similar clustering and length distribution analysis. **This** method **provides constraints on** the depth of fracture penetration **(**still an unanswered problem**)** (Rudolph and Manga, 2009), and demonstrates the prevalence of fractal populations of faults on Enceladus.

The paper is structured as follows: after mapping the distribution of fractures belonging to five different regions of **Enceladus**, we analyze their length distribution and self-similar clustering (Bonnet et al., 2001; Bour et al., 2002, Gudmundsson et al., 2013). We compare the SPT **pattern-fracture** results with literature (Gioia et al., 2007; Smith-Konter and Pappalardo, 2008; Rudolph and Manga, 2009; Olgin et al., 2011, Iess et al., 2014; Yin et al., 2015) to assess the reliability of our approach and, finally, we extended the analysis to all dataset**s** providing the behavior of fracture penetration in the Enceladus ice shell up to 75°N latitude.

3 Case study

We analyzed patterns of fractures located in different regions of the icy satellite **to** which we applied the fractures' length distribution and self-similar clustering analysis, explained in the Method section. We used the Enceladus mosaic from images acquired by the Imaging Science Subsystem (ISS, onboard NASA Cassini spacecraft) that consists of a wide-angle camera and a narrow-angle camera (Porco et al., 2005). The narrow-angle camera **provides** high-resolution images of targets of interest, while the wide-angle camera **allows** a more extended spatial coverage at lower resolution. The global mosaic used as **a** base map is provided by USGS and contains 586 images in various filters (color, green, UV3, and infrared 3)**,** selected for the control network (Becker et al., 2016). Images were selected according to coverage, quality and spatial resolution ranging between 50 and 500 m/px with phase angles less than 120 degrees. Some existing gaps in the global coverage (between 90°N and 50°N in places) were filled with one image from NASA's Voyager 2 spacecraft, which visited Enceladus more than 25 years ago. All the images underwent a high-pass filter to remove low frequency albedo and enhance the surface fractures and structures. The map is projected as equidistant (simple cylindrical) with a scale of 110 m/px at the equator (Fig. 1). The mean radius of Enceladus used for projection of this map is 252 km (Becker et al., 2016).

We mapped fractures in five different regions improving the recently published geological map of Crow-Willard and Pappalardo (2015)**,** following the same definition criteria of their structural interpretation. In particular, we have taken into account the fractures located in well-defined geological units. On these fractured terrains, we improved the mapping of the *wide troughs* and *narrow troughs* (Fig. 1). The *wide troughs* are defined by Crow-Willard and Pappalardo (2015) as relatively long (>100 km long and >2 km wide) curvilinear features in **planar** view, which often

present branched tips and appear rounded smooth in cross section. The *narrow troughs,* commonly shorter than the *wide troughs,* present a width < 2 km and cross cut other geologic units and structures (Crow-Willard and Pappalardo, 2015). Troughs are the most widespread structural feature on the satellite's surface and, in this work, we focused particularly on the narrow ones, being larger in number and most likely related to recent/incipient brittle tensional deformation of the ice shell (Crow-Willard and Pappalardo, 2015). Along with the *narrow troughs,* we also mapped the features interpreted as tension fractures (Yin and Pappalardo, 2015) **with steep walls, almost constant aperture and lateral tips often exposed, that are present in evenly-spaced straight parallel sets**. In our analysis, we **focused particularly** on tension fractures to investigate an interconnected fracture network, which could even work as pathway for cryovolcanic fluids **(Bonini et al., 2010)**.

The five different datasets used in the analysis are the following (Fig. 1):

- Dataset 1 (ds1): region around the South Pole (up to 50°S latitude) with 253 fractures mapped (Fig. 1b);
- Dataset 2 (ds2): region extending mainly in the southern hemisphere**,** centered at longitude value of 175°W (55°S - 10°N latitude, 165°W – 185°W longitude) with 384 fractures mapped (Fig. 1c);
- Dataset 3 (ds3): region extending down from the equator**,** centered at longitude value of 10°W (25°S – 0° latitude, 350°W - 40°W longitude) with 481 fractures mapped (Fig. 1c);
- Dataset 4 (ds4): Regions extending around the equator, more precisely centered at longitude values of 283°W (15°S - 25°N latitude, 265°W – 306°W longitude) with 328 fractures mapped (Fig. 1c);
- Dataset 5 (ds5): northern region centered at longitude value of 330°W (35°N - 75°N latitude, 315°W - 345°W longitude) with 85 fractures mapped (Fig. 1c).

The mapping was carried out with ESRI ArcGis software, calculating the **fractures'** length as well as the barycenter of each fracture in latitude and longitude. To reduce the deformation due to the image projection, we used a sinusoidal projection with a local reference meridian for each equatorial dataset, while a polar stereographic projection was applied for the south polar dataset (see Appendix A).

For the ds1 (South Pole region), which is mainly characterized by iso-oriented wide troughs, we considered fractures inside the central South Polar unit (csp), following the geological map nomenclature of Crow-Willard and Pappalardo (2015). We mapped the narrow branched troughs that crosscut and interact with the TSF, but we **did not consider** the southern curvilinear (cl_3) ring surrounding the SPT (Crow-Willard and Pappalardo, 2015). This region mainly consists **of** a belt of

ridges and troughs that are subparallel to the outer limit of the central SPT, with two Y-shaped branches **that** depart radially from the cl_3 towards the trailing hemisphere. Within these branches, ridges and troughs are present and they appear convex towards the north in planar view (Crow-Willard and Pappalardo, 2015). A slightly complex tectonic history is hypothesized for the cl_3 unit. In particular, strike slip deformation was detected in some areas, mainly in the sub-Saturnian and anti-Saturnian margins (see Yin and Pappalardo, 2015), while compression was identified in the section facing the trailing hemisphere, especially localized on the Y-shaped branches. These features are interpreted as contractional fold and thrust belts that transition into extensional structures to the north, where extensional bookshelf structures were identified in the cl_3 section facing the leading hemisphere (Yin and Pappalardo, 2015). The most likely origin for such a complex structural framework **in** cl_3 is the SPT spread and lateral escape towards the trailing hemisphere, due to the presence of a near South-Pole-centered transient thermal anomaly (Barr, 2008; Yin and Pappalardo, 2015). Although the presence of tension fractures radial to the SPT margin and crosscutting the larger structures was spotted by several authors (Porco et al., 2006; Gioia et al., 2007, Yin and Pappalardo, 2015; Yin et al., 2016), their number is negligible for a fractal clustering analysis. For these reasons, the cl_3 region was not considered in this study.

Ds2 and ds3 were chosen inside the Cratered Plains unit (cp_1). This geologic unit is most likely the oldest one on Enceladus (crater age retention ~4.2 - 4.6 Ga, Porco et al., 2006, Kirchoff and Schenk, 2009) and presents heavily cratered terrain, including **subducted** material and shallow craters **with sizes ranging** between the image resolution and ~35 km (Crow-Willard and Pappalardo, 2015). Cp_1 bears morphologically fresh *narrow-troughs* crosscutting larger craters (up to 30 km) and in **some** places merging pit chains that **suggest an** incipient extension. On the other hand, the presence of few large *wide troughs* suggests important tectonization of the ice crust in the past (Crow-Willard and Pappalardo, 2015). The subdued appearance of part of this unit, especially proximal to the equator (Kirchoff and Schenk, 2009), is thought to be due to accretion by plume material ejected from the TSF in the SPT.

Ds4 is located in the Trailing Hemisphere Terrain (THT) and more specifically in the ridged material (r) region. The (r) unit is dominated by the so-called *dorsa:* **large, smooth, mostly iso-oriented NW-SE ridges of few km in width**, whose origin is likely related either to fluid injection along pre-existing fractures (Spencer et al., 2009) or to pervasive **thrust-blocks** tectonics on the pre-existing striated plains (Pappalardo et al., 2010). This whole area also presents **N-S** oriented narrow and wide troughs crosscutting the dorsa and is surrounded by striated plains (sp) along the equator with ridges and troughs. It is also characterized by a U-shaped region, called Trailing Hemisphere Curvilinear (cl_1), which underwent reshaping under effects of contraction. This latter

region, cl_1, is truncated to the south by the transitional unit (t) characterized by curvilinear troughs. Among these regions, we concentrated our mapping only within the (r) area because of the higher frequency of fracturing and narrow troughs. **We also took into** consideration the ridge fetaures (r) due to their possible origin related to fluid injection along fractures (Spencer et al., 2009) or as a proxy to the presence of faulting due to their rectilinear geometry (Pappalardo et al, 2010).

Extremely low resolution images **in** the North Polar area prevented the mapping of this region, however, we were able to identify and map a fracture dataset (ds5) in the Samarkan Sulci area in the northern part of the trailing hemisphere (Yin and Pappalardo, 2016).

This region was identified as north lineated (nl) terrain located in the trailing hemisphere and presents a smooth terrain dissected by a **N-S** system of narrow troughs and pit chains (Crow-Willard and Pappalardo, 2015). In addition, it was hypothesized that resurfacing from cryovolcanism has affected this area, but mainly from extensional tectonics (Crow-Willard and Pappalardo, 2015).

3 Method

Brittle deformation (faults, fractures, joints) occurs beyond the Earth on many other planets, satellites, and asteroids in the Solar System. Faults on these bodies exhibit the same attributes of fault geometry, displacement–length scaling, interaction and linkage, topography, and strain accommodation as on Earth terrestrial faults, indicating common processes despite environmental differences, i.e. gravity, surface temperature, temperature gradient and tectonic driving mechanisms (e.g., Schultz et al., 2010).

Two main distributions can be used **when analyzing** fault population statistics: size distribution and spatial distribution. The former focuses on the properties of geometric features **such** as fault length or displacement, while the latter analyzes the properties of the whole population **by** relating each fault to others, such as fault density and clustering. Experimental studies on normal fault populations suggest the presence of a lower (L_{co}) and an upper cutoff (U_{co}) in the power law describing the size-distribution of the geometric properties of fractures (Ackermann et al., 2001). In addition, two or more power **laws** have been observed in normal fault population length distributions (e.g. Gudmundsson and Mohajeri, 2013).

Fault length distribution is often used to define the evolution of fault systems (e.g. Soliva and Schultz, 2008; Schultz et al., 2010; Mohajeri and Gudmundsson, 2012; Gudmundsson et al., 2013) and, in particular, two main length distributions are used to describe fault populations:

$$N(>l) = cl^{-a} \qquad (1a)$$

$$N(>l) = \beta e^{-\lambda a} \qquad (1b)$$

where $N(>l)$ is the number of faults with length greater than l, c is the scaling factors and a is the exponent for the power-law distribution (1a), β and λ the parameters of the exponential distribution and a its exponent (1b).

The vertical dimension of **a** faults (height) is nearly proportional to its length and is controlled by the mechanical layering of the crust as long as a sufficiently large contrast in material properties exists between the layers (e.g., Benedicto et al., 2003; Gudmundsson et al., 2010; Soliva and Schultz, 2008). Analysis of fault length distribution in the Main Ethiopian Rift-Afar system (Soliva and Schultz, 2008) show clearly that **small-size**, evenly spaced faults with an exponential length distribution are mainly confined **to** the uppermost mechanical unit (basaltic lava flows). Conversely, the faults, which are characterized by a power law size distribution and whose large-scale **linkages** belong to the border zones (large throw faults), cut the entire brittle crust. Thus two end-**members** for fault length distribution can be identified (e.g., Soliva and Schultz, 2008; Schultz et al., 2010): (i) localized fault systems, with few large faults cutting across the whole crust down to the main mechanical discontinuity, displaying a power-law distribution, and (ii) distributed fault systems, with strain regularly distributed along evenly spaced faults and confined within specific mechanical layers in the crust, displaying an exponential distribution.

The fractures' spatial distribution (i.e. fracture/fault clustering) depends strictly on the spacing of fractures that, in turn, is correlated with the thickness of the fractured medium calculated **for extensional faulting** on the basis of the stress saturation model (Wu and Pollard, 1995; Gross et al., 1995; Ackermann and Schlische, 1997; Schultz et al., 2010). **Linear scaling relationships between fault spacing and thickness of the brittle crust has been also confirmed for strike-slip faults on icy satellites (Yin et al., 2016) as well as for continental scale strike-slip faults on Earth (Zuza et al., 2017).**

A robust way to define how fractures fill space is to analyze their self-similar clustering (Bonnet et al., 2001). The self-similar clustering of fractures is performed for a range of lengths (the size range) between a lower (L_{co}) and an upper cutoff (U_{co}). Mandelbrot (1982) suggested that there are L_{co} and U_{co} for the scale-invariant characteristics of fractures (e.g., spacing, length, density), and **that** these are **a** function of the resolution of the methods used to map and detect fractures (L_{co}) as well as of mechanical layers and rock properties (U_{co}).

Moreover, on Earth**,** both the thickness of sedimentary beds with different mechanical properties (e.g., Gudmundsson et al., 2010) and the crust **is** mechanical layering control the scaling law of fractures and earthquakes (Pacheco et al., 1992; Davy, 1993; Ouillon et al., 1996). The spatial distribution (fracture clustering) of fractures along the East African Rift System (Mazzarini and Isola, 2010) has clearly shown scaling relationships with the crust thickness affected by

faulting, indeed, the thickness of the fractured layer control the dimension of fractures (e.g. Gudmundsson, 2011). **Also in the Pali Aike volcanic fields in the southernmost Patagonia**, the self-similar clustering of fracture traces has scaling relationships with crustal thickness (Mazzarini and D'Orazio, 2003).

The upper cutoffs (U_{co}) for the scale-invariant characteristics of fractures (in this case self-similar clustering) are thus considered directly linked to the mechanical layering of the medium and, hence, in this case reflect the thickness of the fractured layer.

In this work, the spatial distribution (self-similar clustering) of fractures was analyzed by applying the two-point correlation function method to measure the fractal dimension of the fracture population. For a population of *N* points (fracture's trace barycenter) the correlation integral *C(l)* is defined as the correlation sum that accounts for all the points at a distance of less than a given length *l* (Hentschel and Procaccia , 1983; Bour and Davy, 1999, Bonnet et al., 2001).

The term *C(l)* is computed as

$$C(l) = 2\,N(l)/N(N-1) \qquad (2)$$

where *N(l)* is the number of pairs of points whose distance is less than *l*. The fractal distribution of *C(l)* is defined by

$$C(l) \sim c l^{D} \qquad (3)$$

where *c* is a normalization constant and *D* is the fractal exponent. If scaling holds, equation (2) is valid and the slope of the curve in a *log(C(l))* versus *log(l)* diagram yields the fractal exponent (*D*); the higher the *D* value, the less clustered the system. Self-similarity exists in range of distances (*l*), which is defined as size range bounded by L_{co} and U_{co}, where the scaling of *C(l)* with *l* is valid. Within this size range, the linear fit of the curve is well defined and the angular coefficient of the straight line is the fractal exponent D. The local slope is a point by point measure of the slope of the tangent to the curve

$$local\ slope = (\Delta log(C(l)/\Delta log(l)) \qquad (4)$$

where linear fit holds, the curve is a straight line and the local slope (the angular coefficient of the regression line) is constant.

For each analysis, the size range of samples is in turn defined by a plateau in the local slope versus log(l) diagram: the wider the range the better the computation of the power-law distribution (Walsh and Watterson, 1993). The derivation of the cut-offs defining the size range is not trivial, especially when the local slope does not show a regular and wide plateau.

The L_{co} and U_{co} are defined according to the method described in Mazzarini (2004) **by** selecting the wider length range for which the correlation between log(l) and the local slope is greatest. The goodness of fit for fractures' length distribution and the evaluation of the cut-off

estimation for fractures spatial distribution are reported in Appendix B.

4 Results and Discussion

Azimuthal distribution of fractures in ds1 (Figure 2a) has a clear NE-SW trending peak and a secondary narrow ESE-WNW trending peak. The length distribution ranges between 3 and 117 km with an average of 20 km (Table 1) and a maximum frequency ranging from 10 to 15 km (Figure 2b). The cumulative distribution of fracture length (Figure 2c) shows a negative exponential distribution for fractures with length shorter than 22 km (defined as a threshold length l_{th}) and a power-law distribution for fractures with length larger than 22 km (Table 1). This behavior reflects the possible presence of (i) distributed fault systems, with strain regularly distributed along evenly spaced faults and confined within specific mechanical layers in the crust (exponential distribution) and (ii) localized fault systems, with few large faults cutting across the whole crust down to the main mechanical discontinuity (power-law) (e.g., Soliva and Schultz, 2008; Schultz et al., 2010).

Fractures of the ds1 dataset were also analyzed investigating their spatial distribution, clustering and fractal dimension yielding a D exponent in the size range bounded by L_{co} and U_{co}, as explained in the Method section. The spatial distribution shows self-similar clustering (Figure 2d) with D= 1.9633 and U_{co}= 31 km (Table 2).

The L_{co} value is very sensitive to the presence of short fractures in the size distribution, which in turn depends on the image resolution. In this work, due to the low resolution of images, the L_{co} is not considered in the following discussion. The U_{co} has been related to the mechanical discontinuity (i.e., maximum difference in terms of viscosity and stiffness) between different layers and defines the thickness of the fragile crust that is mechanically fractured (Mazzarini and D'Orazio, 2003; Mazzarini and Isola 2010; Mazzarini et al., 2013; Pozzobon et al., 2015).

In the ds1 case, the U_{co} ~31 km represents the depth of fractures' penetration and, in this unique case, it corresponds to the depth of the ocean-ice interface due to the fact that SPT has a very high thermal gradient and fractures are likely to reach the ocean-ice interface. For this reason, we can compare our result to the measurement of the total ice shell thickness obtained from Cassini gravity data (Iess et al., 2014). By analyzing them, it was found that the compensation depth beneath the SPT is between 30 and 40 km, which can be considered as the mean thickness of the ice shell above a liquid ocean extending from South Pole to 50°S (Iess et al., 2014). As the gravitational inverse problem is not formally unique, gravity data were revised and re-interpreted suggesting that: 1) the compensation depth (shell thickness) of Enceladus' global (degree 2) ice shell is 50 km and 2) the compensation depth (shell thickness) beneath the SPT (from J3) remains thinner (approximately 30 km) than the shell at the equator (McKinnon, 2015). Therefore, the U_{co} value for the ds1, 31 ± 3 km (Table 2), is comparable with **the** above gravity-independent estimates.

In addition, we also compare our ds1 result with the current estimates of the brittle ice crust restricted to the SPT terrain, which ranges from 2 km to 35 km (Gioia et al., 2007; Smith-Konter and Pappalardo, 2008). The large diversity of values can be attributed to the different physical processes assumed in different studies to assess the formation of tiger-stripe fractures (hereafter TSF). A minimum of 5 km is found modeling shear heating along the TSF (Roberts and Nimmo, 2008), while Smith-Konter and Pappalardo (2008) and Olgin et al. (2011) show that the SPT ice shell is between 2 and 40 km from the effect of tidal stress acting on TSF. The fractures penetration is treated by Rudolph and Manga, (2009) finding that the SPT ice shell is likely to be thinner than 25 km. Investigating spacing between TSF, Gioia et al., (2007) and Helfenstein and Porco (2015) inferred the thickness of the SPT ice shell to be 35 and 5 km respectively, but without providing a quantitative mechanical reason. In this framework, our result are slightly in agreement with previous brittle ice crust estimates and, in particular, we are coherent with recent results of Yin et al., (2016) that estimate a 30 km SPT brittle ice shell thickness on the basis of the formation of evenly spaced TSF in the SPT.

After assessing the reliability of our approach thanks to SPT results, we applied the length size distribution analysis and the fractal clustering approach to the other four selected regions to estimate the fractures behavior and penetration depth.

The fractures size-distribution analysis for the other regions (Table 1) show length distributions characterized by negative exponential distributions for fractures with length**s** shorter than the l_{th} and a power law distribution for fractures with length**s** larger than l_{th} (Table 1 and Figure 3). From this analysis we found that the threshold length, l_{th}, varies between 10 and 36 km (Table 1).

Fracture populations with two different size-distributions, as derived for the **complete** data set, have **also** been **observed on Earth, where two different size distributions have been** extensively studied on field (Cowie et al., 1994, Scholtz et al., 1993) by analogue (Ackermann et al., 2001) and numerically modeling (Soliva et al., 2006, Cowie et al., 1995). The transition between negative exponential and power-law size-frequency distributions (SFD) appears to be related both to fault growth and linkage in a vertically confined medium. Ackermann et al., (2001) reported that the negative exponential SFD is related to nucleation of new faults occurring during incipient phases of extension, when mechanical layering **is not an** influence (due to the small size). The exponential behavior is also related to the saturation of a vertically-confined system in which large regularly-spaced faults dominate and accommodate most of the strain (e.g., Schultz et al., 2010; Cowie *et al*., 1994; Ackermann et al., 2001). Before the saturation, the interaction of fractures and the **consequent** linkage/growth process overcomes the nucleation of new faults

providing a power-law SFD behaviour (Cowie et al., 1995).

In Enceladus' case, it results that the fracture systems under study can represent the whole evolutional time-frame starting from fractures' formation and incipient extension (negative exponential) to present day (power-law with almost constant steepness), but before the saturation point. Specifically, the two length size distributions probably reflect both the first stages of deformation (negative exponential) and the presence of a mechanical/rheological layering, which is determined by a power-law behavior that is related to fault-spanning throughout the entire brittle shell (Schultz et al., 2010; Ackermann et al., 2001).

The length threshold (l_{th}), discriminating the two different fractures' length behavior can represent the effects of: (i) the depth above which tensile stresses exist and where fractures with a length shorter than l_{th} are likely confined (Rudolph and Manga, 2009), and (ii) the development and growth of fractures with length larger than l_{th} penetrating the entire brittle ice shell (likely up to brittle-ductile ice transition), probably due to a higher strain rate.

The quantitative values of the thickness of **the** penetrated brittle ice shell are given through the self-similar clustering analysis. The results are reported in Table 2 and displayed in Figure 4. **In more** detail, the **depth of fractures' penetration** found for the ds2, ds3, ds4 and ds5 **are** 42.5 ± 2.5, 32 ± 4, 43.5 ± 3.5 and 69.9 ± 3.3, respectively (Table 2).

Figure 5 gives an overview of the results showing the plot of *log(l) vs. local slope* for each analyzed region. Data here are stacked in order to show their similarit**ies** and differences. **The differently-dashed vertical bands represent the U_{co} values that define the depth of the mechanical discontinuity of Enceladus' ice shell which is the depth to which fractures penetrate the ice layer. In Enceladus' case, the brittle ice likely rests upon a ductile ice layer that may mark the transition to the ocean and deforms in agreement with planetary strain rates and thermal gradients (Roberts and Nimmo, 2008). The behavior of the brittle-ductile ice of Enceladus' crust is not yet totally understood, hence, the portion of the crust investigated by fractures' penetration correspond to the mechanical discontinuity of the ice shell and not necessarily to its full extent (i.e., the depth of the ocean).**

From Figure 5, it is shown that the ds1 brittle ice shell thickness is similar to the one of the region containing the ds3, which extends in latitude from 25°S to the equator, while the ds2 and ds4 present a brittle ice shell thickness of about 43-44 km. The difference between these findings is quite small considering errors included in the analysis (see Table 2), while ds5 provides a totally different value **of** ~70 km.

In conclusion, the depth of fractures' penetration ranges between 31 and 44 km from the South Pole up to 25°N latitude, while it increases in the northern region up to 70 km. The

large discrepancy between this latter region and the other**s** can be attributed to the still-unsolved mechanism causing the tectonic dichotomy between the very active SPT and inactive North Polar region (Showman et al., 2013).

These results give new insight **into** the depth of the base of the brittle ice and the mechanical/rheolog**ical** layering on icy satellite (which is still an **unresolved** problem) (Rudolph and Manga, 2009), and demonstrate the prevalence of fractal populations **of** faults on Enceladus.

5 Conclusions

The structural geology approach used in this work reveals new insight regarding the thickness of brittle ice in multiple regions of Enceladus. Exploring the main geometrical properties of fractures, we performed length distribution (Soliva and Schultz, 2008; Schultz et al., 2010) and self-similar clustering analysis (Bonnet et al., 2001) on the selected datasets.

We revealed two different length distributions, probably reflecting the effect of the depth distribution of the tensile stresses and the depth of the brittle-ductile ice boundary.

The self-similar clustering analysis allowed us to quantify the thickness of fractured (brittle) ice shell. Firstly, we consider**ed** the dataset corresponding to the SPT because its results allow a direct comparison with literature. We found agreement between our results, which imply a brittle ice layer of 31 km, and both the gravity independent estimates revealed by Cassini data (Iess et al., 2014; McKinnon, 2015) and those reported by different studies regarding the mechanical formation of TSF in SPT (Gioia et al., 2007; Smith-Konter and Pappalardo, 2008; Olgin et al., 2011, Yin et al., 2015). Then, applying the results to the other four selected regions (ds2, ds3, ds4 and ds5), we cover the satellite up to northern latitudes. We estimate that the **thickness of the** brittle ice shell of Enceladus ranges between 31 and 44 km from the South Pole up to 25°N latitude, while it increases in the northern region reaching a value of 70 km. This latter result reflects the tectonic contrast characterizing the two poles that is still an **unresolved** problem. Starting from geological evidence (fractures), we provide new knowledge about the depth of fracture penetration and mechanical/rheolog**ical** layering on Enceladus, which is still a debated problem (Rudolph and Manga, 2009), and demonstrate the prevalence of fractal populations of faults. This structural approach can be of interest because of the possible application on other icy bodies whose fracture penetration depth**'s are** still unknown, such as the Galilean satellites.

Acknowledgments

We thank Agust Gudmundsson and two anonymous referees for important and constructive comments that lead to a substantial improvement of the paper.

This research was supported by the Italian Space Agency (ASI) through the ASI-INAF agreement no.2013-056-RO. We made use of the ArcGIS 10.2 software to perform the presented analysis. We are grateful to R.T. Pappalardo and E.N. Crow-Willard to provide us the ArcGIS Enceladus geological map project.

The authors thank Zachariah Milby of the University of Colorado in Boulder for a careful read of the manuscript.

Appendix A. Surface curvature contribution

In order to minimize the effect of the satellite's curvature in the fracture datasets analysis, we use a sinusoidal projection for areas around the equator and a polar stereographic projection for the SPT. Since the fractal clustering analysis works in 2D, the curvature effect of a small body such as Enceladus (252 km in radius) must be taken into account. Indeed, it is not sufficient a proper projection to avoid deformation of lineaments and distances throughout the datasets, hence, the knowledge of the curvature influence on the U_{co} final results (for fracture datasets around 200 km in size) is mandatory. We selected a smaller portion of the datasets used, where the curvature effect is negligible, to verify the consistency of our measurements and results.

As a rule of thumb, by selecting smaller datasets, we applied the same proportions between the dataset's size and planet radius used in the published fractal clustering analysis related to Earth crustal thickness, whose calculation is strongly consistent with independent measurements (i.e. geophysical data such as inversion of **the** local gravity field and seismic tomography). Specifically, previous works (Mazzarini et al., 2013; Mazzarini et al., 2010) analyzed the fractures in the Main Ethiopian Rift system where the maximum size of vents and fractures systems ranges between 600 km and 800 km. A similar type of analysis was performed for a ~400 km system in the Mexican volcanic belt (Mazzarini et al., 2013).

Thus, considering the Earth**'s** radius equal to 6371 km and the average size of the studied systems of 600 km, the size of the analyzed dataset should be 10-13% of the satellite radius **on average**.

In other words, **with** Enceladus' radius of 252 km, the maximum size of the studied fractured surface portion that has a negligible curvature should be ~40 km.

Therefore, we selected 29 lineaments in a smaller region (~45x50 km^2) of the ds1 area (Fig. A1a), while for the equatorial region we sampled a portion of the ds3 area (Fig. A1b) whose

maximum size is ~40x45 km^2 and bears the most densely fractured terrain among all datasets. We chose a subset just southern to the intersection between the equator and the reference meridian of the sinusoidal projection obtaining a dataset of 60 fractures.

These sub-datasets contain fewer records, nonetheless, a sample of ~50 points is sufficiently large to perform a fractal clustering analysis (Clauset et al., 2009).

For these two subsets the same fractal clustering analysis as the whole dataset was performed, checking the scaling of the U_{co} and L_{co} thresholds.

The Fig. A1c reports the local slopes of log (l) vs log C(l) plots for ds1 and ds3 datasets and subsets. It is clear that all the U_{co} values obtained are consistent and comparable (especially for the ds1 fractures that bear only 29 samples), hence, the influence of curvature in using dataset involving a larger area is assumed within the errors of the estimations (Fig. A1).

Appendix B. Goodness of fit for fractures' length distribution and cut-off estimation for fractures spatial distribution.

A log-log plot that yields a straight line is regarded an indication that the data follow a power-law distribution. **However,** even if the data follow a power law distribution, it does not follow that the power law necessarily provides the best model or fit for the data (Mohajeri and Gudmundsson, (2012)). This is the case for our fractures' lengths distributions. Indeed, we found that a single power law **did not fit the data well**. Following the Clauset e al. (2009) approach, we obtained a power law distribution for length**s** above a well-defined threshold finding a higher R^2 value for each dataset, in comparison to other distribution**s** (such as exponential). The value of R^2 may be regarded as a measure of the goodness of fit, but when difference in the R^2 values between different distributions is not large enough, **an** alternative test might be performed.

This is not our case, since the R^2 value is high enough to rule out alternative distribution above a threshold length. However, we simply calculate the p-value using the available codes of Clauset et al. (2009), with the program Matlab and the statistical programming language R, to strengthen our conclusion. We obtained a p-value for power law distribution for each dataset that is larger than 0.1 (as shown in Table B1), hence the power law is not ruled out (Clauset et al. (2009)).

Dataset	**l_{th}**	**alpha**	**p-value**
Ds1	22	2.339	0.98
Ds2	20	3.856	0.78
Ds3	10	2.875	0.72
Ds4	36	4.947	0.46
Ds4	14	2.486	0.42

Table B1. For each dataset we report the power law fit above a threshold length and the p-value**.**

The estimation of cutoff position**s** for fractures' spatial distribution is empirical; as an example we analyze the dataset 3 (ds3) consisting of 481 fracture traces. The barycenter of the traces have been computed and their self-similar clustering analyzed applying equations (1) to (3). The results are shown in the plot of l vs. $C(l)$ and local slope (Fig. B1a) and all possible values of R^2 vs. *size range* ($\Delta log(l)$) have also been computed (Fig. B1b); points inside the blue box (Fig. B1b) represent the maximum size ranges (that is $U_{co} - L_{co}$) that have the highest possible R^2 values. The comparison with the local slope is important because large size ranges with relatively high R^2 values are also computed for **non-constant** local slopes (i.e. not power law fit, see portion A in Fig. B1a). The points in the R^2 *vs.* $\Delta log(l)$ plot along with the variation of the *local slope* with l indicate that the optimal size range has a L_{co} varying between 2-2.1 km and a U_{co} varying between 28-36 (average 32) km; the errors in the computation of the L_{co} are about 10% and for the U_{co} vary from 6% up to 12%. From equation (2) the corresponding fractal exponent D is computed **for** the size range defined by the average values of cutoffs with errors < 2%.

The sampling of fracture population is affected by "truncation" and "censoring" effects. Short fractures are incompletely observed as the limit of resolution of the observation methods is approached (truncation), causing a shallowing of slope of the distribution trend at the lower end of the scale range. Long fractures tend to be incompletely sampled because they pass outside the observed region (censoring), causing an artificial steepening of the distribution trend at the upper end of the scale range. According to Bour et al. (2002), spatial correlation analysis of fracture is valid whatever the point used to define fracture location (barycenter, fracture tips, or any point taken at random in the fracture). The reason comes from the fact that the derivation of **a** two-point correlation dimension is statistically dominated by the numerous small fractures, for which the error in the determination of the precise spatial location is relatively insignificant. Consequently, the censoring effects (fractures that intersect the system boundaries), which have to be explicitly taken into account when deriving the length distribution model (Pickering et al., 1995), did not affect the derivation of the fractal dimension. Thus, the definition of the upper cut off (U_{co}) does not suffer **from** censoring effects. Truncation derives from the system's resolution when acquiring data and it may produce an underestimation of small size objects and small range spatial distributions (i.e. objects closer than the minimum resolution are not distinguished), which in turn affects the definition of the lower cutoff (L_{co}). Other sources of errors derive from the number of samples acquired and the accuracy in their spatial location (i.e. errors in mapping fracture traces and the relative barycenter). Mazzarini and Isola (2010) show that removing a random sample of 20% from large (i.e. >200 points) datasets does not affect the estimation of fractal dimension (less than 0.01% of variation) and the error introduced into the estimation of the cut-offs is less than 1%–2%.

Mazzarini et al., (2013) also tested the effect of uncertainties in point locations by adding random errors (in the 0–100 m, 0–300 m and 0–500 m ranges) to the sampled points. In this test, the added errors are as high as five to twenty five times that of the coarsest image resolution we used to locate points. The 0–100 m errors randomly added to the point locations generate fractal exponents and cut offs value identical to those computed for the original dataset. In the case of 0–500 m random errors, the resulting fractal exponent is 3% higher than that computed for the original dataset, and the cut offs are very similar to those computed for the original dataset (Mazzarini and Isola, 2010). The minimum number of samples required for extracting robust parameter estimates must be between 50 and 150, as reported in literature (Bonnet et al., 2001; André-Mayer and Sausse, 2007; Clauset et al., 2009).

References

Ackermann, R.V., and Schlische, R.W., (1997), Anticlustering of small normal faults around larger faults: Geology, v. 25, p. 1127–1130, doi:10.1130/0091-7613.

Ackermann, R.V., Schlinsche, R.W., and Withack, M.O., (2001), The geometric and statistical evolution of normal fault systems: An experimental study of the effects of mechanical layer thickness on scaling laws: Journal of Structural Geology, v. 23, p. 1803–1819, doi: 10.1016/S0191-8141(01)00028-1.

André-Mayer, A.-S., and Sausse, J., (2007), Thickness and spatial distribution of veins in a porphyry copper deposit, Rosia Poieni, Romania: Journal of Structural Geology, v. 29, p. 1695–1708, doi: 10.1016/j.jsg.2007.06.010.

Barr, A.C., (2008). Mobile lid convection beneath Enceladus' south polar terrain. *Journal of Geophysical Research: Planets*, *113*(E7).

Becker, T.L., Bland, M. T., Edmundson, K. L., Soderblom, L. A., Takir, D., Patterson, G. W., Collins, G.C., Pappalardo, R.T., Roatsch, T., and Schenk, P.M., (2016). Completed Global Control Network and Basemap of Enceladus. In *Lunar and Planetary Science Conference* (Vol. 47, p. 2342).

Benedicto, A., Schultz, R.A. and Soliva R., (2003). Layer thickness and shape of faults. Geophysical Research Letters, 30, 20, 2076, doi:10.1029/2003GL018237.

Bonini, Marco, and Francesco Mazzarini (2001). Mud volcanoes as potential indicators of regional stress and pressurized layer depth. Tectonophysics 494.1, 32-47.

Bonnet, E., Bour, O., Odling, N.E., Davy, P., Main, I., Cowie, P., and Berkowitz, B., (2001), Scaling of fracture systems in geological media: Reviews of Geophysics, v. 39, p. 347–383, doi: 10.1029/ 1999RG000074.

Bour, O., and Davy, P., (1999), Clustering and size distribution of fault patterns: Theory and measurements: Geophysical Research Letters, v. 26, p. 2001–2004, doi:10.1029/1999GL900419.

Bour, O., Davy, P., Darcel, C., and Odling, N., (2002), A statistical scaling model for fracture network geometry, with validation on a multiscale mapping of a joint network (Hornelen Basin, Norway): Journal of Geophysical Research, v. 107, p. 2113, doi: 10.1029/2001JB000176.

Clauset, A., C. R. Shalizi, and M. E. J. Newman (2009), Power-law distri- butions in empirical data, SIAM Rev., 51, 661–703. doi:10.1137/ 070710111.

Collins, G. C., & Goodman, J. C. (2007). Enceladus' south polar sea. *Icarus*, *189*(1), 72-82.

Cowie, P. A., Malinverno, A., Ryan, W. B., & Edwards, M. H. (1994). Quantitative fault studies on the East Pacific Rise: A comparison of sonar imaging techniques. *Journal of Geophysical Research: Solid Earth*, *99*(B8), 15205-15218.

Cowie, P. A., Sornette, D., & Vanneste, C. (1995). Multifractal scaling properties of a growing fault population. *Geophysical Journal International*, *122*(2), 457-469.

Crow-Willard, E. N., & Pappalardo, R. T. (2015). Structural mapping of Enceladus and implications for formation of tectonized regions. *Journal of Geophysical Research: Planets*, *120*(5), 928-950.

Davy, P., (1993), On the frequency-length distribution of the San Andreas fault system: Journal of Geophysical Research, v. 98, p. 12,141–12,151, doi:10.1029/93JB00372.

Gioia, G., Chakraborty, P., Marshak, S., & Kieffer, S. W. (2007). Unified model of tectonics and heat transport in a frigid Enceladus. *Proceedings of the National Academy of Sciences*, *104*(34), 13578-13581.

Gross, M.R., Fischer, M.P., Engelder, T., and Greenfield, R.J., (1995), Factors controlling joint spacing in interbedded sedimentary rocks: Integrating numerical models with field observations from the Monterey Formation, USA, in Ameen, M.S., ed., Fractography: Fracture topography as a tool in fracture mechanics and stress analysis: Geological Society [London] Special Publication, v. 92, p. 215–233.

Gudmundsson, A., Simmenes, T.H., Larsen, B. and Philipp, S.L., (2010). Effects of internal structure and local stresses on fractyre propagation, deflection and arrest in fault zones. Journal of Structural Geology, 32, 1643-1655.

Gudmundsson, A., (2011) Rock Fractures in Geological Processes. Cambridge University Press, Cambridge, UK, pp 594.

Gudmundsson, A., and Mohajeri, N., (2013). Relations between the scaling exponents, entropies,

and energies of fracture networks. Bull.Géol. France, 2013, 184, 4, 377-387.

Gudmundsson, A., De Guidi, G., and Scudero, S., (2013). Length-displacement scaling and fault growth. Tectonophysics, 608, 1298-1309.

Hansen, C., Esposito, L., Stewart, A., Colwell, J., Hendrix, A., Pryor, W., Shemansky, D., West, R., (2006), Enceladus' Water Vapor Plume. Science. 311, 1422–1426. doi:DOI:10.1126/science.1121254.

Helfenstein, P., & Porco, C. C. (2015). Enceladus' geyser: relation to geological features *Astronomical Journal*, *150*(3), 96.

Hentschel, H. G. E., and I. Proccacia (1983), The infinite number of generalised dimensions of fractals and strange attractors, Physica D: Nonlinear Phenomena, 435-444.

Iess, L., Stevenson, D.J., Parisi, M., Hemingway, D., Jacobson, R. a, Lunine, J.I., Nimmo, F., Armstrong, J.W., Asmar, S.W., Ducci, M., Tortora, P., 2014. The gravity field and interior structure of Enceladus. Science 344, 78–80. doi:10.1126/science.1250551.

Jenness, J. 2013. Polar Plots and Circular Statistics: Extension for ArcGIS. Jenness Enterprises.

Kirchoff, M. R., & Schenk, P. (2009). Crater modification and geologic activity in Enceladus' heavily cratered plains: Evidence from the impact crater distribution. *Icarus*, *202*(2), 656-668.

Mandelbrot, B.B., (1982), The Fractal Geometry of Nature: San Francisco, Freeman, 468 p.

Mazzarini F., D'Orazio, M. (2003). Spatial distribution of cones and satellite-detected lineaments in the Pali Aike Volcanic Field (southernmost Patagonia): Insights into the tectonic setting of a Neogene rift system: Journal of Volcanology and Geothermal Research, v. 125, p. 291–305, doi: 10.1016/S0377-0273(03)00120-3.

Mazzarini, F., (2004), Volcanic vent self-similar clustering and crustal thickness in the northern Main Ethiopian Rift: Geophysical Research Letters, v. 31, p. L04604, doi: 10.1029/2003GL018574.

Mazzarini, F., Isola, I. (2010). Monogenetic vent self-similar clustering in extending continental crust: Examples from the East African Rift System: Geosphere, v. 6, p. 567–582, doi: 10 .1130/GES00569 .1.

Mazzarini, F., Keir, D., Isola, I. (2013) Spatial relationship between earthquakes and volcanic vents in the central-northern Main Ethiopian Rift. *Journal of Volcanology and Geothermal Research* 262, 123–133.

McKinnon, W. B. (2015), Effect of Enceladus's rapid synchronous spin on interpretation of Cassini gravity. Geophys. Res. Lett., 42, 2137–2143.

Mohajeri, N., and Gudmundsson, A., (2012). Entropies and Scaling Exponents of Street and Fracture Networks. Entropy, 14, 800-833.

Olgin, J. G., Smith‐Konter, B. R., & Pappalardo, R. T. (2011). Limits of Enceladus's ice shell thickness from tidally driven tiger stripe shear failure. *Geophysical Research Letters*, *38*(2).

Ouillon, G., Castaing, C., and Sornette, D., (1996), Hierarchical geometry of faulting: Journal of Geophysical Research, v. 101, p. 5477–5487, doi:10.1029/95JB02242.

Pacheco, J.F., Scholz, C.H., and Sikes, L.R., (1992), Change in the frequency-size relationship from small to large earthquakes: Nature, v. 355, p. 71–73, doi:10.1038/355071a0.

Pappalardo, R. T., Crow-Willard, E., & Golombek, M. (2010). Thrust Faulting as the Origin of Dorsa in the Trailing Hemisphere of Enceladus. In *Bulletin of the American Astronomical Society* (Vol. 42, p. 976).

Patthoff, D.A., Kattenhorn, S., (2011). A fracture history on Enceladus provides evidence for a global ocean. Geophys. Res. Lett. 38. doi:10.1029/2011GL048387.

Pickering, G., J. M. Bull, and D. J. Sanderson, (1995), Sampling power-law distributions, Tectonophysics, 248, 1 –20.

Porco, C. C. *et al.* (2005), Cassini imaging science: Instrument characteristics and anticipated scientific investigations at Saturn. *Space Sci. Rev.* 115, 363–497.

Porco, C.C., Helfenstein, P., Thomas, P.C., Ingersoll, A.P., Wisdom, J., West, R., Neukum, G., Denk, T., Wagner, R., Roatsch, T., Kieffer, S., Turtle, E., McEwen, A., Johnson, T. V, Rathbun, J., Veverka, J., Wilson, D., Perry, J., Spitale, J., Brahic, A., Burns, J.A., Delgenio, A.D., Dones, L., Murray, C.D., Squyres, S., (2006), Cassini observes the active south pole of Enceladus. Science, 311, 1393–401. doi:10.1126/science.1123013

Porco, C., DiNino, D., Nimmo, F., (2014). How the Geysers, Tidal Stresses, and Thermal Emission Across the South Polar Terrain of Enceladus Are Related. Astron. J. 148. doi:10.1088/0004-6256/148/3/45.

Pozzobon, R., Mazzarini, F., Massironi M., Marinangeli, L. (2015). Self-similar clustering distribution of structural features on Ascraeus Mons (Mars): implications for magma chamber depth. *Geological Society, London, Special Publications*, 401, doi:10.1144/SP401.12

Roberts, J. H., & Nimmo, F. (2008). Tidal heating and the long-term stability of a subsurface ocean on Enceladus. *Icarus*, *194*(2), 675-689.

Rudolph, M. L., & Manga, M. (2009). Fracture penetration in planetary ice shells. *Icarus*, *199*(2), 536-541.

Schultz, R.A., Soliva, R., Okubo, & C.H., Mège D. (2010). Fault populationsons. In: *Planetary Tectonics*, edited by Thomas R. Watters and Richard A. Schultz. Cambridge University Press, Cambridge, 457-510."

Scholz, C. H., Dawers, N. H., Yu, J. Z., Anders, M. H., & Cowie, P. A. (1993). Fault growth and

fault scaling laws: preliminary results. *Journal of Geophysical Research: Solid Earth*, *98*(B12), 21951-21961.

Showman, A. P., Han, L., & Hubbard, W. B. (2013). The effect of an asymmetric core on convection in Enceladus' ice shell: Implications for south polar tectonics and heat flux. *Geophysical Research Letters*, *40*(21), 5610-5614.

Smith-Konter, B., & Pappalardo, R. T. (2008). Tidally driven stress accumulation and shear failure of Enceladus's tiger stripes. *Icarus*, *198*(2), 435-451.

Soliva, R., Benedicto, A., & Maerten, L. (2006). Spacing and linkage of confined normal faults: importance of mechanical thickness. *Journal of Geophysical Research: Solid Earth*, *111*(B1).

Soliva, R., and Schultz, R.A., (2008). Distributed and localized faulting in extensional settings: Insight from the North Ethiopian Rift–Afar transition area. Tectonics, 27, TC2003, doi:10.1029/2007TC002148.

Spencer, J.R., Pearl, J.C., Segura, M., Flasar, F.M., Mamoutkine, A., Romani, P., Buratti, B.J., Hendrix, a R., Spilker, L.J., Lopes, R.M.C., (2006). Cassini encounters Enceladus: background and the discovery of a south polar hot spot. Science (80-.). 311, 1401–5. doi:10.1126/science.1121661

Spencer, J. R., Barr, A. C., Esposito, L. W., Helfenstein, P., Ingersoll, A. P., Jaumann, R., McKay, C.P., Nimmo, F. and Waite, J. H. (2009). Enceladus: An active cryovolcanic satellite. In *Saturn from Cassini-Huygens* (pp. 683-724). Springer Netherlands.

Thomas, P. C., Tajeddine, R., Tiscareno, M. S., Burns, J. A., Joseph, J., Loredo, T. J., Helfenstein, P., Porco, C. (2016). Enceladus's measured physical libration requires a global subsurface ocean. *Icarus*, *264*, 37-47.

Walsh, J.J., and Watterson, J., (1993), Fractal analysis of fracture pattern using the standard box-counting technique: Valid and invalid methodologies: Journal of Structural Geology, v. 15, p. 1509–1512, doi: 10.1016/0191- 8141(93)90010-8.

Wu, H., and Pollard, D.D., 1995, An experimental study of the relationships between joint spacing and layer thick- ness: Journal of Structural Geology, v. 17, p. 887–905, doi: 10.1016/0191-8141(94)00099-L.

Yin, A., & Pappalardo, R. T. (2015). Gravitational spreading, bookshelf faulting, and tectonic evolution of the South Polar Terrain of Saturn's moon Enceladus. *Icarus*, *260*, 409-439.

Yin, A., Zuza, A. V., & Pappalardo, R. T. (2016). Mechanics of evenly spaced strike-slip faults and its implications for the formation of tiger-stripe fractures on Saturn's moon Enceladus. *Icarus*, *266*, 204-216.

Zuza, A.V., Yin, A., Lin, J., & Sun, M. (2017). Spacing and strength of active continental

strike-slip faults. Earth Planetray Science Letters, 457, 49-62.

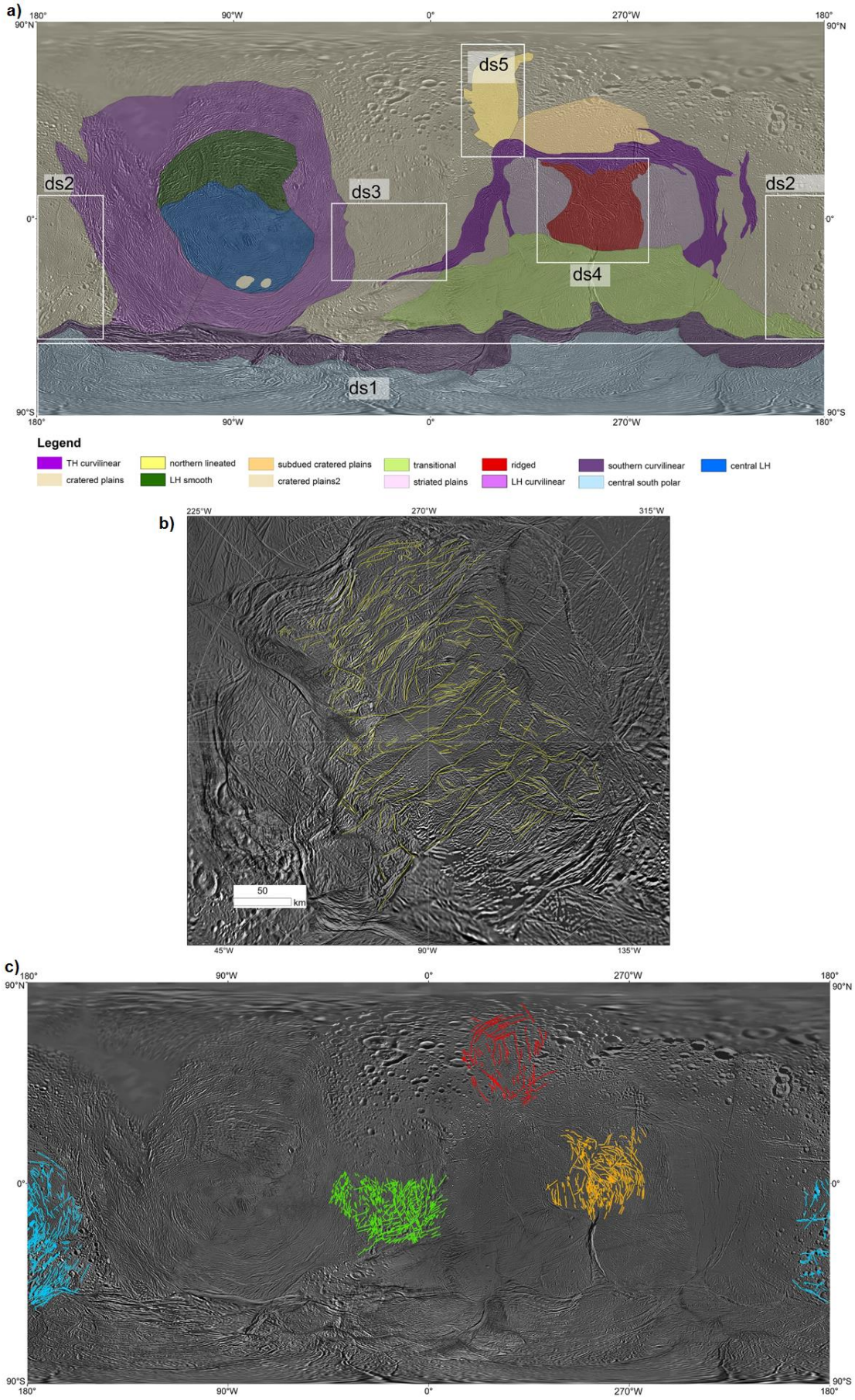
a)
180°
90°W
0°
270°W
180°
90°N
90°N
ds5
ds2
ds3
ds2
0°
0°
ds4
ds1
90°S
90°S
180°
90°W
0°
270°W
180°
Legend
TH curvilinear
cratered plains
northern lineated
LH smooth
subdued cratered plains
cratered plains2
transitional
striated plains
ridged
LH curvilinear
southern curvilinear
central south polar
central LH
b)
225°W
270°W
315°W
50
km
45°W
90°W
135°W
c)
180°
90°W
0°
270°W
180°
90°N
90°N
0°
0°
90°S
90°S
180°
90°W
0°
270°W
180°
Legend
ds1
ds2
ds3
ds4
ds5

Figure 1: The five different regions used in this work. **a)** Simple cylindrical global image mosaic of Enceladus produced by the Cassini ISS team (Credit: NASA/JPL/Space Science Institute) with superimposed the geological map provided by Crow-Willard and Pappalardo (2015). The dataset (ds) within the five regions selected for our analysis are outlined on the map. **b)** The ds1 (region around the South Pole) is projected in polar stereographic projection to reduce the image deformation. The number of features used in the analysis is 253. **c)** The ds2, ds3, ds4 and ds5 are projected in sinusoidal projection using a local reference meridian. The number of fractures analyzed in these regions are 384, 481, 328 and 84, respectively.

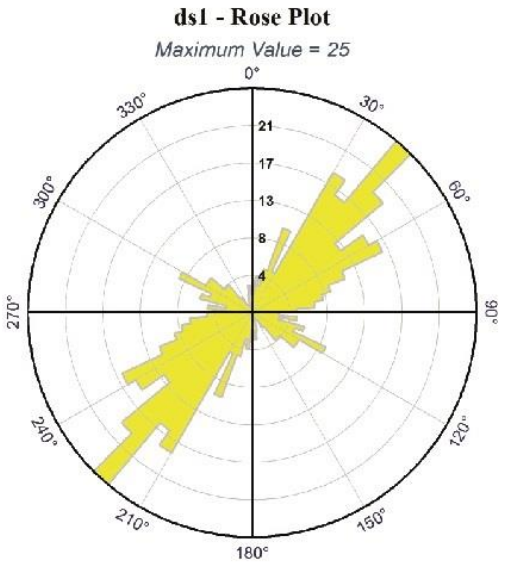
ds1 - Rose Plot
Maximum Value = 25
0°
30°
60°
90°
120°
150°
180°
210°
240°
270°
300°
330°
21
17
13
8
4

a)

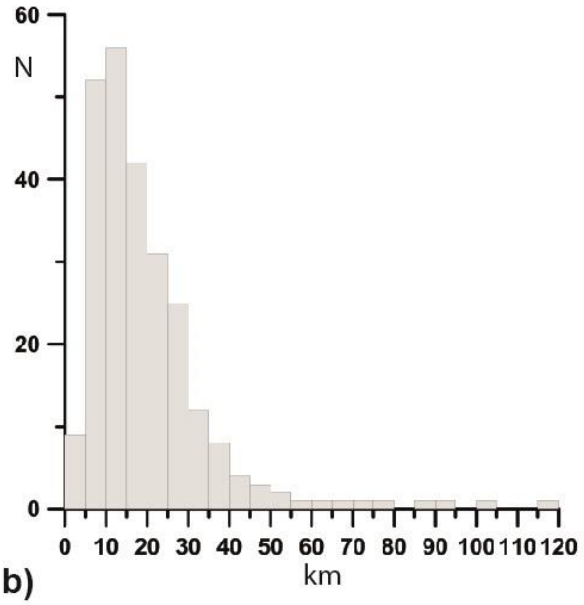
N
60
40
20
0
0 10 20 30 40 50 60 70 80 90 100 110 120
km

b)

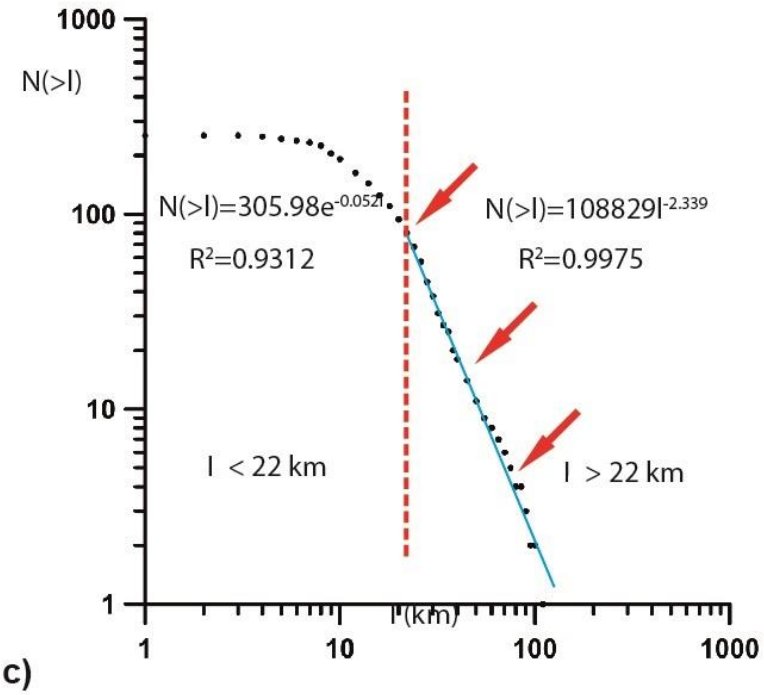
N(>l)
1000
100
10
1
N(>l)=305.98e-0.052l
R²=0.9312
N(>l)=108829l-2.339
R²=0.9975
l < 22 km
l > 22 km
l (km)
1
10
100
1000

c)

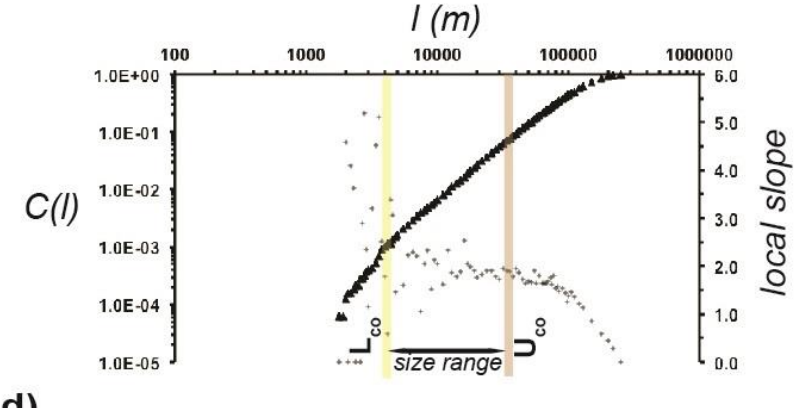
l (m)
100
1000
10000
100000
1000000
C(l)
1.0E+00
1.0E-01
1.0E-02
1.0E-03
1.0E-04
1.0E-05
local slope
6.0
5.0
4.0
3.0
2.0
1.0
0.0
Lco
Uco
size range

d)

Figure 2: Fracture length distribution and self similar clustering of the ds1 data set. a) Rose diagram (Jenness, 2013) showing the azimuthal distribution of fractures. b) Histogram of fracture length distribution (bin size= 5 km). c) Cumulative distribution of fractures' length (Table 1): fractures shorter than the threshold length (l_{th} = 22 km, red dashed vertical line) fit well with a negative exponential distribution, while fractures larger than 22 km (red arrows) fit with a power law distribution. d) Self-similar clustering analysis for each dataset considered (log log plot of C(l) vs. l, according to equation 3), crosses represent the local slope (see equation 4); the colored strips are the range of values for L_{co} (yellow strip) and the U_{co} (brown strip) that define the size range of the fractal distribution. The slope of the curve is the fractal exponent D computed in the size range defined by the plateau in the log(l) vs. local slope plot. The portion A of the plot, at the right of the U_{co}, show a clear descending trend of the local slope thus indicating that, although with a relatively high R^2 value, the relation between $C(l)$ and l in the log-log space is not linear.

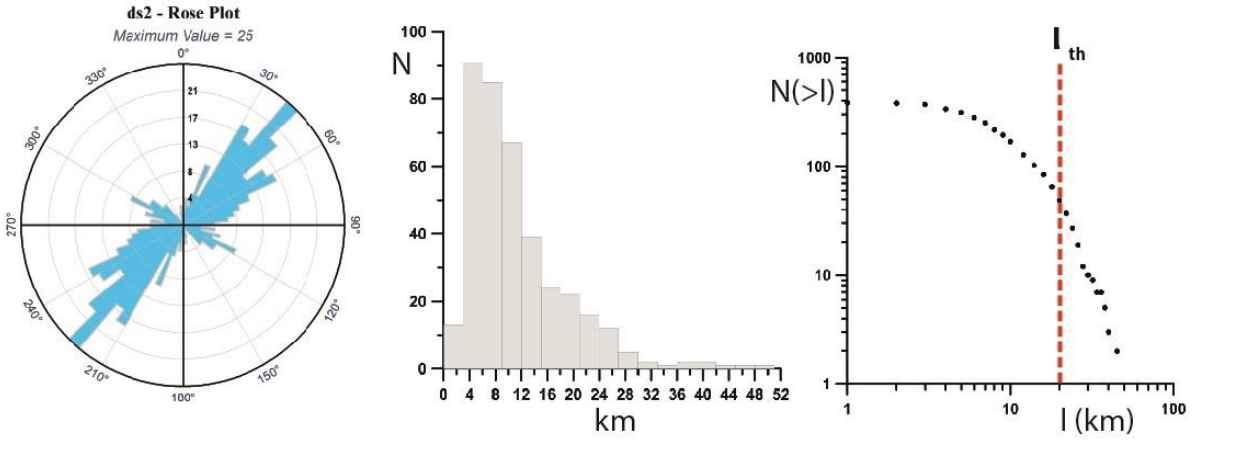
ds2 - Rose Plot
Maximum Value = 25
N
km
N(>l)
l (km)
l th

a)

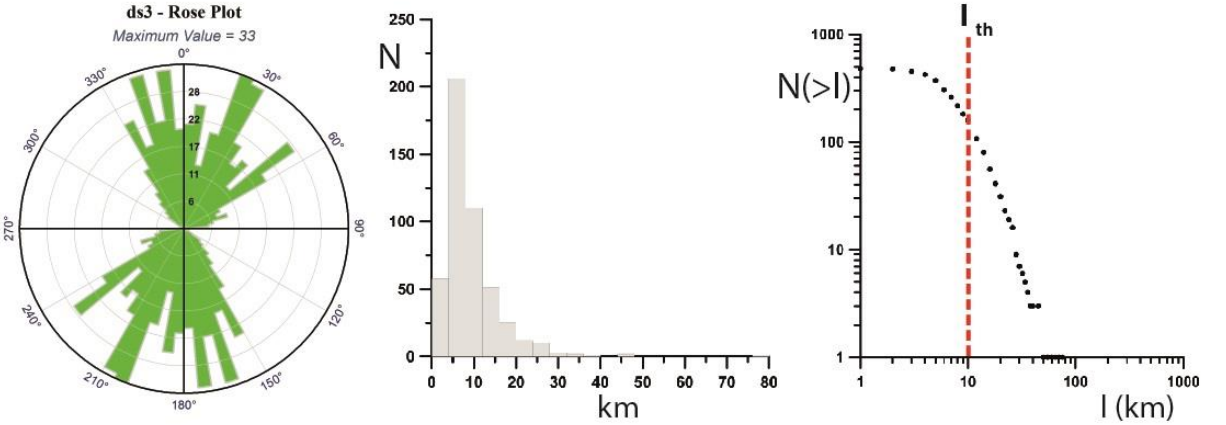
ds3 - Rose Plot
Maximum Value = 33
N
km
N(>l)
l (km)
l th

b)

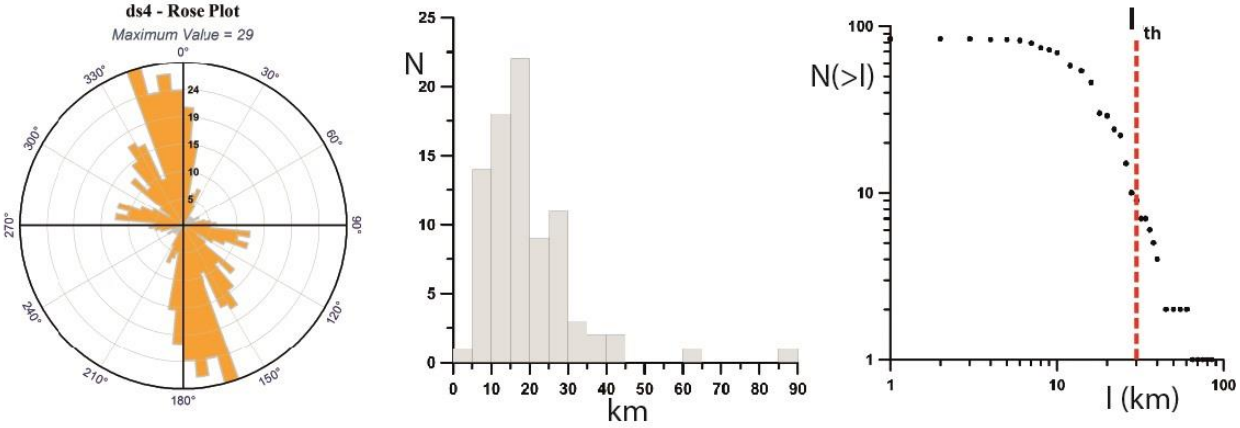
ds4 - Rose Plot
Maximum Value = 29
N
km
N(>l)
l (km)
l th

c)

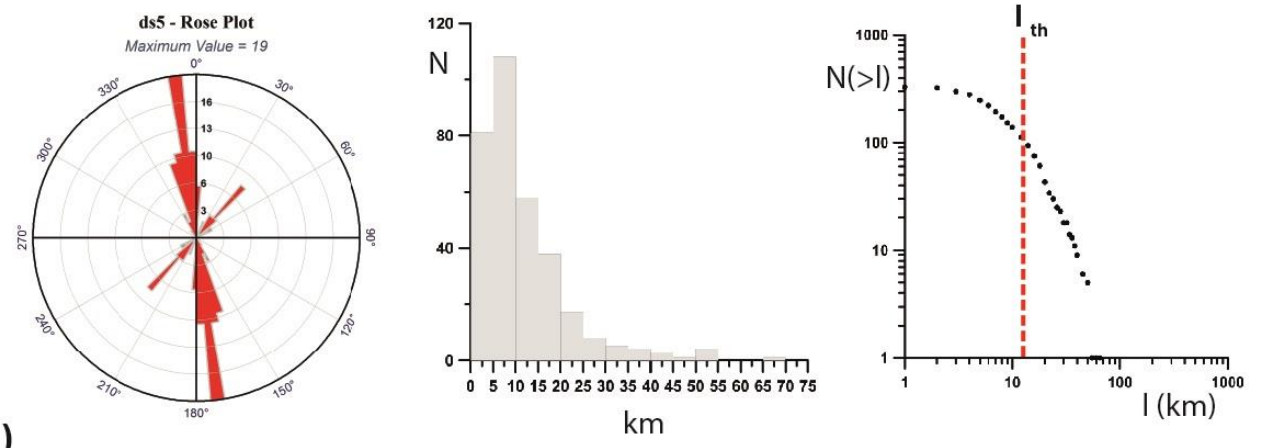
ds5 - Rose Plot
Maximum Value = 19
N
km
N(>l)
l (km)
l th

d)

Figure 3: Length distribution of sampled fracture data sets (Table 1). a) ds2 data set. Left panel: rose diagram (Jenness, 2013) showing the azimuthal distribution of fractures; Central panel: histogram of fracture length distribution (bin size= 4 km). Right panel: cumulative distribution of fractures' length: fractures shorter than the threshold length (l_{th} = 20 km, red dashed vertical line) fit a negative exponential distribution, while fractures longer than 20 km (red arrows) fit with a power law distribution. b) ds3 data set. Left panel: rose diagram (Jenness, 2013) showing the azimuthal distribution of fractures; Central panel: histogram of fracture length distribution (bin size= 4 km). Right panel: cumulative distribution of fractures' length: fractures shorter than the threshold length (l_{th} = 10 km, red dashed vertical line) fit a negative exponential distribution, while fractures longer than 10 km (red arrows) fit with a power law distribution. c) ds4 data set. Left panel: rose diagram (Jenness, 2013) showing the azimuthal distribution of fractures; Central panel: histogram of fracture length distribution (bin size= 5 km). Right panel: cumulative distribution of fractures' length: fractures shorter than the threshold length (l_{th} = 36 km, red dashed vertical line) fit a negative exponential distribution, while fractures longer than 36 km (red arrows) fit with a power law distribution. d) ds5 data set. Left panel: rose diagram (Jenness, 2013) showing the azimuthal distribution of fractures; Central panel: histogram of fracture length distribution (bin size= 4 km). Right panel: cumulative distribution of fractures' length: fractures shorter than the threshold length (l_{th} = 14 km, red dashed vertical line) fit a negative exponential distribution, while fractures longer than 14 km (red arrows) fit with a power law distribution.

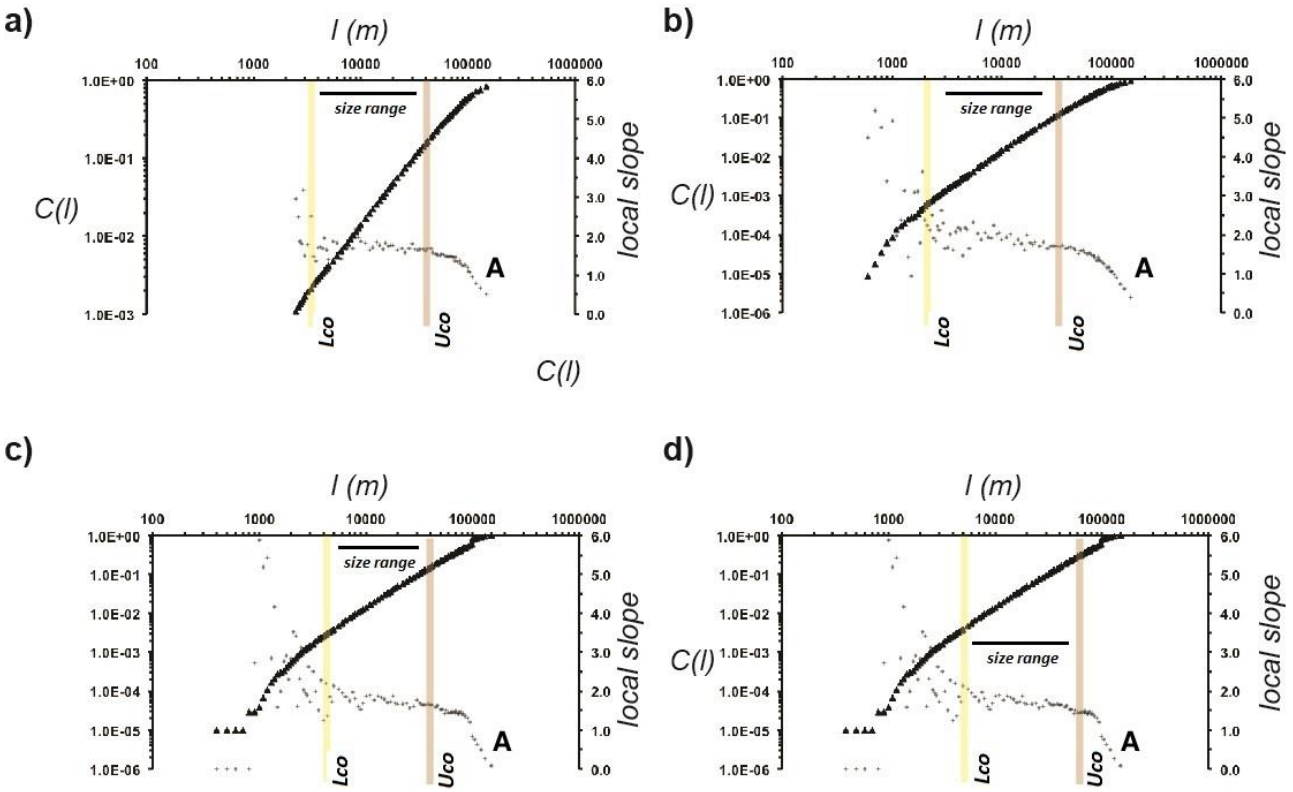

Figure 4: Self-similar clustering analysis for each dataset considered (log log plot of C(l) vs. l, according to equation 3), crosses represent the local slope (see equation 4); the colored strips are the range of values for L_{co} (yellow strip) and the U_{co} (brown strip) that define the size range of the fractal distribution. The slope of the curve is the fractal exponent *D* computed in the size range defined by the plateau in the log(l) vs. local slope plot. The portion A of the plot, at the right of the U_{co}, show a clear descending trend of the local slope thus indicating that, although with a relatively high R^2 value, the relation between *C(l)* and *l* in the log-log space is not linear. The plots correspond to: **a)** ds2, **b)** ds3, **c)** ds4, and **d)** ds5.

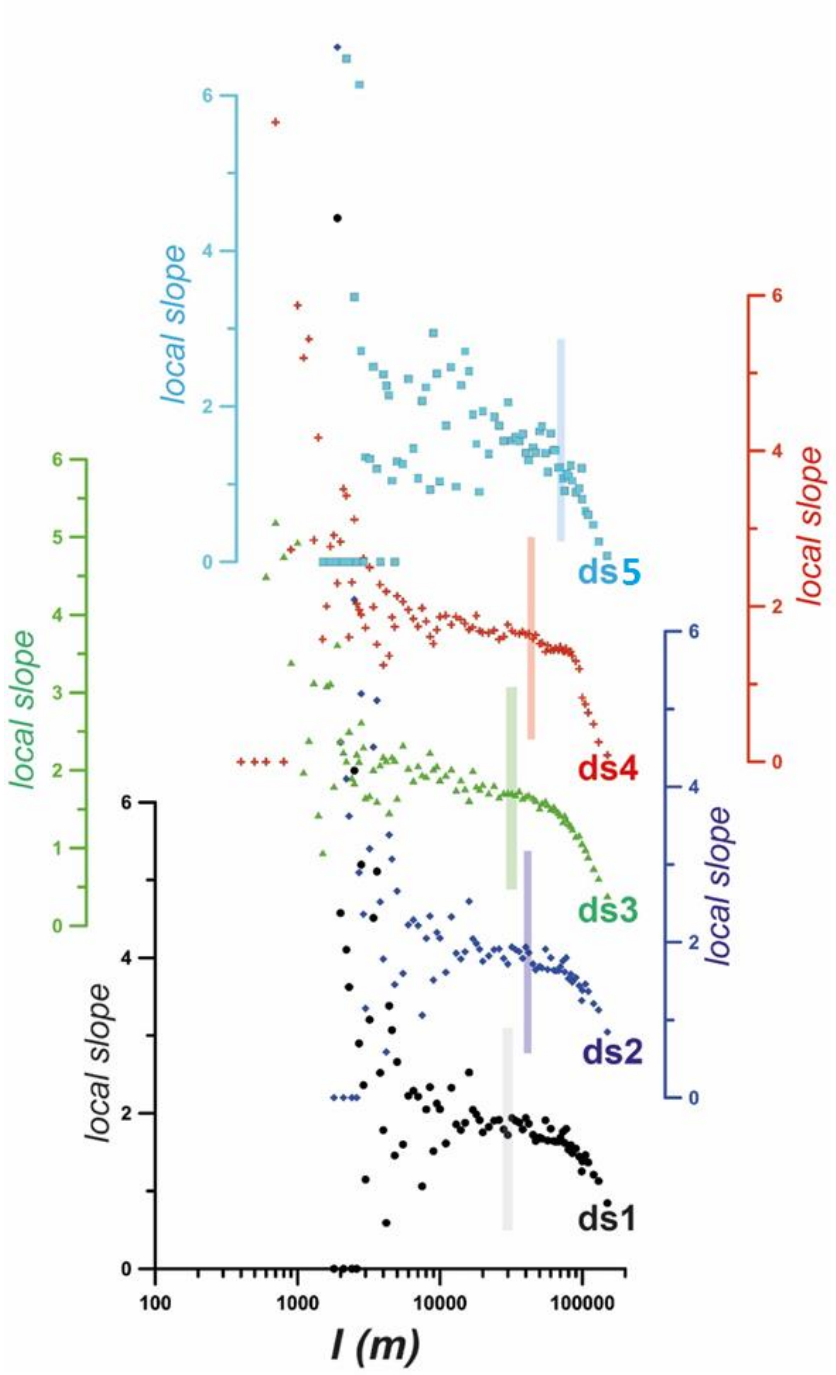

Figure 5: Plot of *log l vs. local slope* for all datasets considered in the analysis. Data are represented by black dots, blue diamonds, green triangles, red crosses and light blue squares for the ds1, ds2, ds3, ds4 and ds5, respectively. The plot compares the estimates of the ice brittle crust thickness found for all different regions which ranges from 31 km to 44 km for the first four dataset. On the other hand, for the ds5, we found a different value of about 70 km.

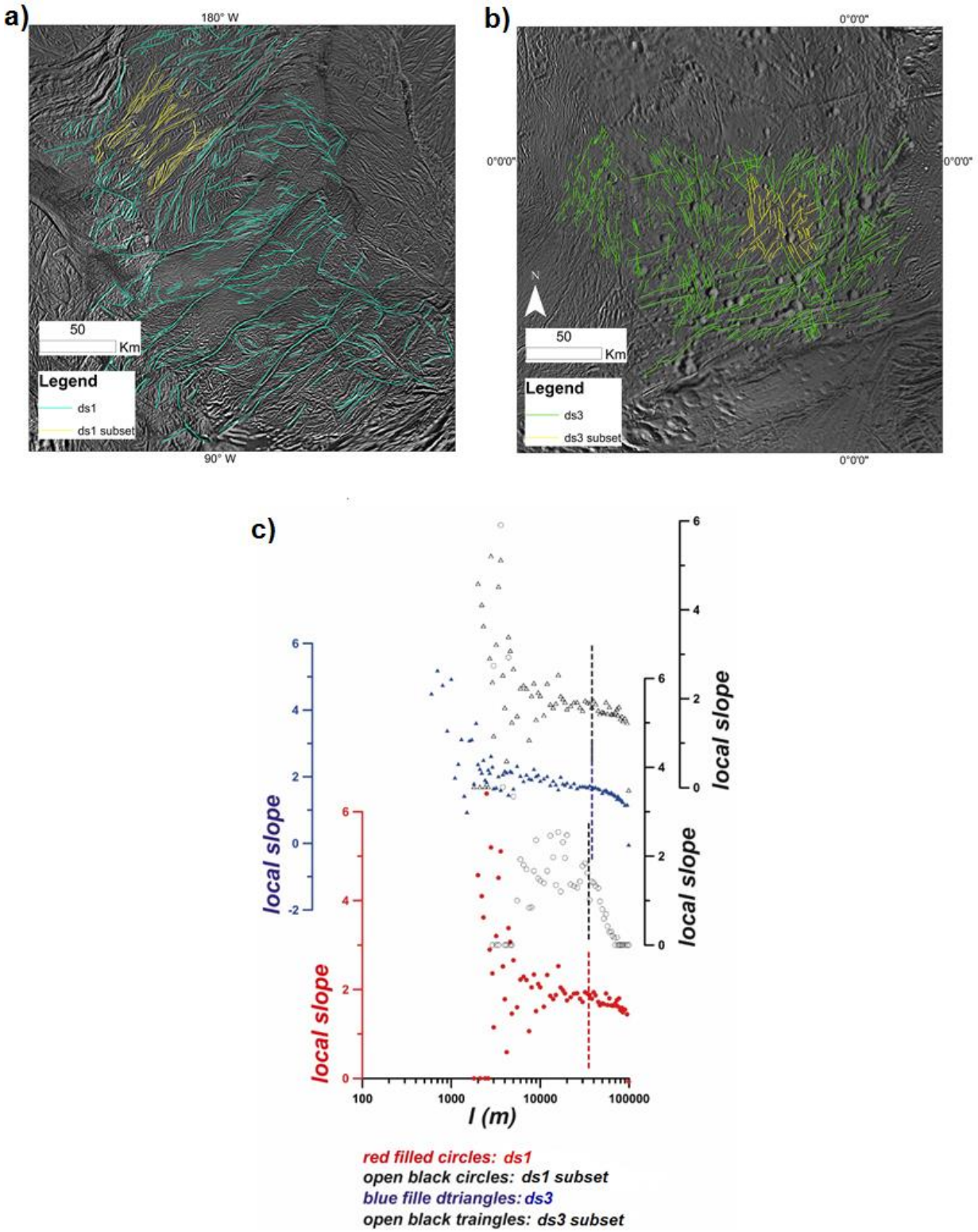

Figure A.1: Self-similar clustering applied to subsets of initial data **a)** The ds3 mapped fractures are shown in green, while the analyzed subset is in yellow; **b)** The ds1 mapped fractures are shown in

blue, while the analyzed subset in yellow. **c)** Plot of *log l vs. local slope* for all datasets considered in the analysis. The dashed lines represent the values of U_{co} for each dataset and relative subset, returning comparable values.

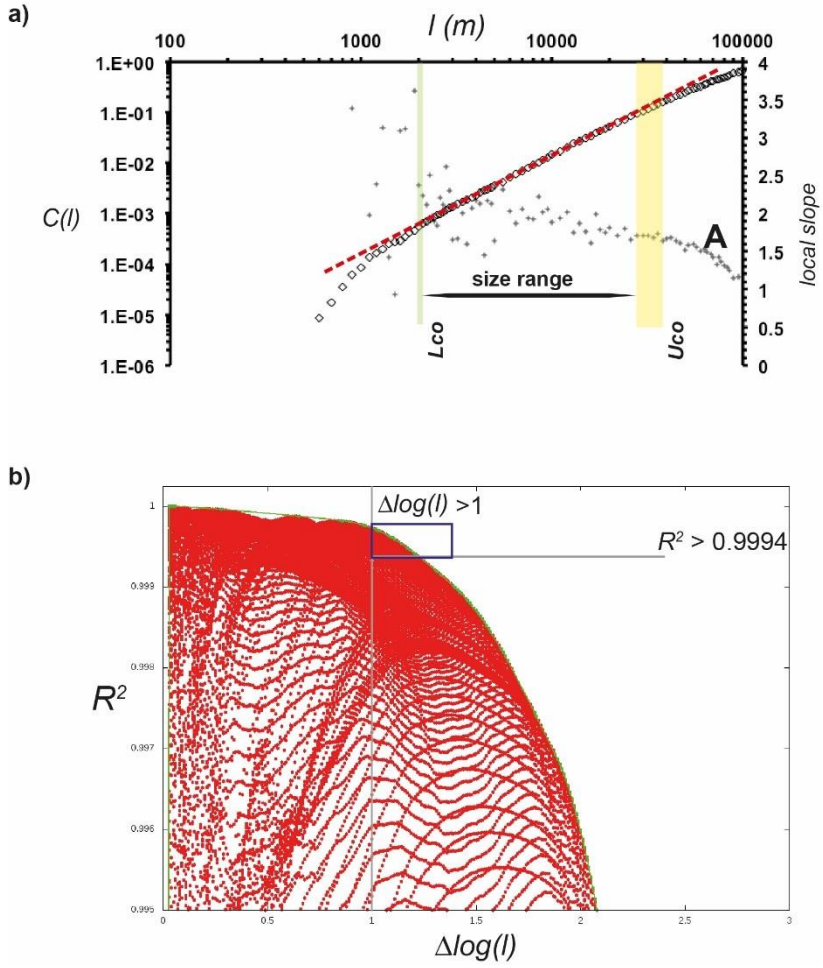

Figure B.1: a) Log log plot of *C(l)* vs. *l* according to equations (1)-(2), crosses represent the local slope (3); the colored strips are the range of values for L_{co} (pale green strip) and the U_{co} (yellow strip) that define the size range of the distribution. The slope of the curve (red dashed line) is the fractal exponent *D*; the portion A of the plot, at the right of the U_{co}, show a clear descending trend of the local slope thus indicating that although with a relatively high R^2 value the relation between *C(l)* and *l* in the log-log space is not linear. b) Plot of all possible *Δlog(l)* (i.e. size range) and R^2 values, the green line marks the border of the distribution; the vertical and horizontal grey lines are the lower boundaries of the space where *Δlog(l)* > 1 and R^2 > 0.9994; the point located along the green line inside the blue box correspond to the position where cut offs satisfying the condition are met.

Table 1: Parameters of length distribution (size-distribution) of fractures for each region under study.

Data set	n	l range (km)	av l (km)	l_{th} (km)	Distributions N(>l)	
					$l < l_{th}$	$l > l_{th}$
ds1	253	3 - 117	20	22	$305.98e^{-0.052L}$ $R^2 = 0.9312$	$108829L^{-2.339}$ $R^2 = 0.9975$
ds2	384	2 – 49	11	20	$523.75e^{-0.116L}$ $R^2 = 0.9912$	$5x10^6L^{-3.856}$ $R^2 = 0.9825$
ds3	481	1 – 79	9	10	$645.39e^{-0.134L}$ $R^2 = 0.9567$	$142376L^{-2.875}$ $R^2 = 0.9762$
ds4	328	1 – 70	12	36	$400.92e^{-0.106L}$ $R^2 = 0.9961$	$7x10^8L^{-4.947}$ $R^2 = 0.9127$
ds5	84	4 - 86	19	14	$97.32e^{-0.04L}$ $R^2 = 0.8914$	$43234L^{-2.486}$ $R^2 = 0.9775$

N: number of fractures; l range: max and min fractures' length; av l: average fracture length; l_{th}: threshold length

Table 2: Parameters of spatial distribution (self similar clustering) of fractures for each region under study.

Data set	Longitude range	Latitude range	n	D	R^2	U_{co} (km)
ds1	0°W-360°W	90°S – 50°S	253	1.9633± 0.03	0.9995	31 ± 3
ds2	165°W – 185°W	55°S – 10°N	384	1.7426 ± 0.01	0.9998	42.5 ± 2.5
ds3	350°W – 40°W	25°S – 0°	481	1.9322 ± 0.03	0.9995	32 ± 4
ds4	265°W – 306°W	15°S – 25°N	328	1.7704 ± 0.02	0.9994	43.5 ± 3.5
ds5	315°W -345°W	35°N-75°N	84	1.7263 ± 0.01	0.9979	69.9 ± 3.3

N: number of samples; D: fractal exponent of fractures self-similar clustering; R^2: goodness of fit; U_{co}: upper cut-off